

Spatial Bifurcations in the Generic N–NDR Electrochemical Oscillator with Negative Global Coupling: Theory and Surface Plasmon Experiments[†]

F. Plenge,^{||} Y.-J. Li,^{||,§} and K. Krischer^{*,||,‡}

Fritz-Haber-Institut der Max-Planck-Gesellschaft, Faradayweg 4-6, 14195 Berlin, Germany, and Physik Department, Technische Universität München, James-Frank-Strasse 1, 85748 Garching, Germany

Received: December 21, 2003; In Final Form: March 29, 2004

Pattern formation during the oscillatory reduction of IO_4^- at a rectangular gold film electrode was investigated by means of surface plasmon microscopy. Several one-dimensional spatial symmetry breakings were observed when a negative global coupling (NGC) was imposed by partially compensating the electrolyte resistance, using a negative impedance device. Respective theoretical investigations of the prototype electrochemical oscillator with an N-shaped current–potential characteristic (N–NDR), corresponding to the IO_4^- reduction, are presented. A complete picture of the spatial bifurcations reproducing the symmetry breakings at a fixed NGC strength is given. The agreement between experiment and model is further emphasized by numerical simulations that revealed a state with double broken symmetry, which we termed asymmetric standing wave. Furthermore, the theoretical studies allow for identification of patterns that arise, owing to a complex interplay of the nonlinear kinetics and unavoidable nonuniformities in the experimental setup. Due to the general nature of the oscillator studied, the observed effects are expected to be representative for N–NDR oscillators under NGC.

1. Introduction

Owing to the importance of a global feedback for a system's dynamics, studies employing global coupling in reaction–diffusion systems were undertaken during the past decade using a variety of model systems, e.g., catalytic reactions,^{1–10} metal and semiconductor devices,^{11,12} biological systems,¹³ and the Belousov–Zhabotinsky reaction, where the global coupling can be light induced.¹⁴ The interest in these studies is two-fold. (1) Methods for the control of complex dynamics often employ global feedback mechanisms.^{15–22} (2) Intrinsic global coupling is present in various systems, in particular, in reactions at interfaces, including heterogeneously catalyzed reactions under UHV conditions,²³ as well as electrochemical reactions.²⁴ Driven by theoretical and experimental studies by Ertl et al.,²⁵ the CO oxidation on Pt developed into a prototype system for the study of the influence of global coupling on pattern formation and its application to control it.^{19,20,26,27}

The bifurcation scenarios leading to the basic spatio-temporal patterns in reaction–diffusion systems under global coupling (e.g., pulses, standing waves, and stationary domains) are well understood since most of the respective solution branches originate from homogeneous solutions. The structural changes in the dynamics that yield more complex patterns in globally coupled reaction–diffusion systems are, in contrast, mostly unknown. Exceptions are selected examples (e.g., an electrochemical and a semiconductor system which each possess an S-shaped current–potential characteristic^{28,29} and, again, the CO oxidation under UHV conditions).³⁰

Electrochemical pattern formation is decisively influenced by the control of the reaction via the external applied voltage or

current, and it is this control that introduces a global coupling into the system.^{31–33} A global coupling acting on a variable, u , is called negative, or desynchronizing, if the dynamics depend on a term of the form $\alpha(\langle u \rangle - u)$ and if α is negative. The brackets denote the spatial average, which, in its general form, is given by $\langle u \rangle = A^{-1} \int_A g(x)u(x) dx$, with a strictly positive, normalized weight function, $g(x)$. A denotes the area of the respective domain. The origin of this terminology becomes clear if one considers the system to be in the homogeneous steady state, $u(x) = u^{\text{ss}}$. A small perturbation of u at a certain location to more positive values causes $\langle u \rangle - u < 0$ in the region of the perturbation. Thus, if $\alpha < 0$, the perturbation will increase further. Accordingly, this type of global coupling enhances spatial perturbations and is called desynchronizing. We define *strict* global coupling as a global coupling which couples all locations with the same strength, i.e., the average is not weighted, $g(x) \equiv 1$.

Negative global coupling (NGC) acting on an electrochemical system was studied previously using a close reference electrode (RE), which introduces the NGC.^{31,32,34–42} Reported experimental results include the observation of the remote triggering of waves and typical patterns, such as pulses, stationary domains, and standing wave-type anti-phase oscillations. A symmetric position of the pointlike RE can only be realized in setups using a quasi one-dimensional (1d) ring working electrode (WE). If two-dimensional (2d) electrodes are used in conjunction with a close RE, the stationary electric field distribution at the WE will be nonuniform, and strict global coupling cannot be realized. Studies with desynchronizing global coupling using a close pointlike RE and a disk WE are discussed in refs 34, 40, and 42.

A new formulation of the global coupling term in the double-layer dynamics derived recently facilitates experiments with strict NGC using 2d WEs.^{43–45} Employing a negative impedance device (NID) (similar to the common mode of ohmic drop

[†] Part of the special issue “Gerhard Ertl Festschrift”.

* Corresponding author. Email address: krischer@ph.tum.de.

^{||} Fritz-Haber-Institut der Max-Planck-Gesellschaft.

[‡] Physik Department, Technische Universität München.

[§] Present address: Department of Chemistry, West Virginia University, P.O. Box 6045, Morgantown, WV 26506.

compensation provided by most commercial potentiostats), electrochemical pattern formation in two spatial dimensions under strict NGC can be investigated. (Conceptually similar setups are also used in semiconductor systems where a negative external resistance is employed. The negative external resistance does not have a comparable physical analogue, as in the electrochemical systems.^{12,46})

It was demonstrated that the insertion of an external series resistor with negative impedance manifests itself in the evolution equation of the double-layer potential in exactly the same way as if the same absolute resistance would be compensated by a close RE in a setup with ring-shaped working and counter electrodes (CE).

Thus, the motivation to study the prototype N-shaped current–potential characteristic (N–NDR) oscillator under NGC using a 2d WE is two-fold. (1) A complete picture of the spatial bifurcations as a function of one bifurcation parameter for a certain nonlinear system will be presented. Herewith, the origin of more complex spatio-temporal patterns is clarified, employing methods from nonlinear dynamics. Among these patterns are previously unreported spatio-temporal motions, which we term asymmetric standing waves. (2) Experiments investigating electrochemical pattern formation in two spatial dimensions with strict NGC by employing a NID are presented for the first time. Using these results, the new formulation of the double-layer dynamics can be tested by close comparison of the experimental data with respective theoretical calculations.

The most prominent examples of electrochemical oscillators with N–NDR are the electro-dissolution reactions of metals with an active/passive transition. The double-layer potential, denoted by ϕ_{DL} , plays the role of the activator in N–NDR systems, i.e., a positive feedback mechanism in ϕ_{DL} is in effect on the branch of negative differential resistance (NDR). The negative feedback necessary for the occurrence of oscillations is provided by a chemical variable. In this contribution, the reduction of IO_4^- at a Au(111)-film WE was chosen since its homogeneous dynamics displays, to a large extent, typical N–NDR features. Additionally, changes in the reaction current are accompanied by changes in the surface plasmon resonance angle, allowing us to monitor reactivity patterns with a surface plasmon microscope (SPM).^{45,47}

This paper is organized as follows. In the next section, the surface plasmon imaging experiments are described. The electrochemical and optical setups are introduced briefly, and the obtained spatio-temporal data as a function of the applied voltage are given. The theoretical description is presented in the Theory section. The prototype N–NDR oscillator under NGC in 1d with no-flux boundary conditions is introduced, and the results of the bifurcation analysis and simulations are given. (Note that, to the best knowledge of the authors, all previous studies used periodic boundary conditions.)

In section 4, the experimental and theoretical data are discussed and compared. Respective conclusions are drawn in the last section. Calculations of a technical nature are compiled in the Appendix.

2. Experiments

2.1. Experimental Setup. Adsorbate or potential patterns at the electrode/electrolyte interface were imaged with a home-built SPM. The top view of the setup is depicted in Figure 1a. The WE consisted of a 50 nm thick gold film that was evaporated onto a glass plate (B270, Schott), which was pre-covered with a 2 nm Cr layer for better adhesion. The plate was brought into optical contact with a glass prism. A Teflon mask was used to press the WE–prism assembly to the

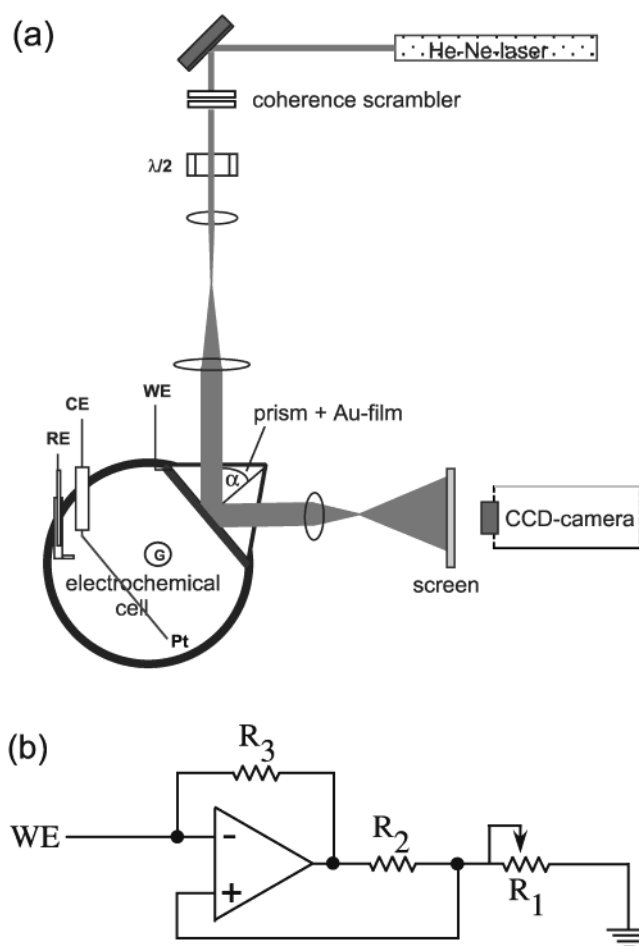


Figure 1. (a) Top view of the experimental setup with SPM and the electrochemical cell. (b) Negative impedance device that was inserted between the WE and the potentiostat.

electrochemical cell, resulting in a contact area between electrode and electrolyte of $30 \times 8 \text{ mm}^2$. Note that the entire electrode area was surrounded by the vertical walls of the Teflon mask and the glass cell (which amounted together to about 7–8 mm in thickness), such that there was no conductor/insulator transition in the plane of the WE. In this way, the complications in the dynamics that arise when the electrode is surrounded by insulating material in the same plane⁴⁸ were kept to a minimum.

The optical part of the SPM consisted of a He–Ne laser (632.8 nm), a coherence scrambler (a rotating sheet of scattering paper that was fixed between two glass plates), a $\lambda/2$ -plate for fast switching between s- and p-polarized light, a combination of lenses to broaden the laser beam, allowing the illumination of the electrode from behind by a parallel, p-polarized beam, imaging lenses, a screen, and a charge-coupled device (Dalsa with a full-frame transfer architecture) connected to an image processing board. The optical data were stored simultaneously with current and potential. In general, recorded images were distorted, owing to the Gaussian laser profile and other optical imperfections in the path, resulting in a position-dependent illumination intensity. To correct for any inhomogeneities in the optical illumination, the images were processed in the following way. For each pixel the maximum and minimum intensities within a series of images were determined. If the difference exceeded a preset value, which represented the noise level, the intensity was scaled to an interval of 0–256; otherwise it was set to 0. Subtracting a background image or taking the differences of successive images gave similar results, but with lower dynamics.

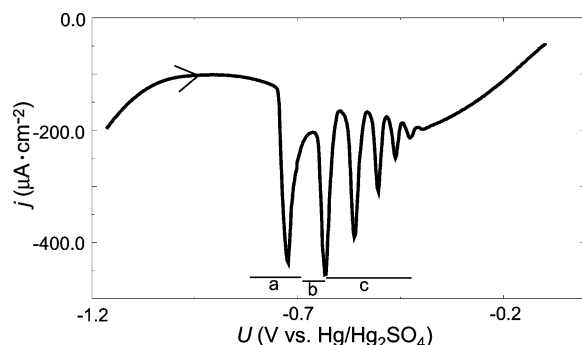


Figure 2. Current–voltage curve recorded during a positive (backward) voltage scan (scan rate 50 mV/s, $R_{\Omega} = 1 \text{ k}\Omega$, $R_e = -800 \text{ }\Omega$; electrolyte: 3 mM NaIO_4 , 2 mM NaClO_4). The regions a–c correspond to the voltage intervals at which the respective patterns displayed in Figures 4a–c were observed.

The electrochemical cell was made up of a cylindrical glass compartment with a rectangular opening in the side wall for the connection to the WE (s.a.). The CE consisted of a Pt wire bent to a rectangular spiral of about the same size as the WE. It was aligned parallel to the WE to ensure a minimum distortion of the electric field in the electrolyte, since any nonuniformity of the electric field influences pattern formation. The distance between the WE and the CE was approximately 5 cm. The RE was placed behind the CE. Due to geometric constraints, the RE was positioned close to one side of the CE rather than symmetrically, which introduced some lateral inhomogeneity (s.b.). The RE was a $\text{Hg}/\text{Hg}_2\text{SO}_4/\text{K}_2\text{SO}_4$ (sat.) electrode ($E_0 = 650 \text{ mV vs SHE}$); all potentials in this section are given with respect to this electrode. An argon inlet was in the center of the cell; continuous Ar bubbling during the experiments provided an enhanced transport of IO_4^- ions, which was necessary to maintain sufficiently large and nearly stationary reaction rates.

The Au film electrode was flame annealed in a butane flame to a reddish glow for 1–2 min and subsequently cooled in air. The procedure was repeated 4–5 times, after which the CV in 0.1 M HClO_4 resembled the one of a Au(111) electrode,⁴⁵ suggesting that the film has, indeed, a high degree of (111)-oriented terraces. The electrolyte solutions were prepared from NaIO_4 and NaClO_4 salts (Sigma Aldrich, 99.8%, and Merck, pA qualities, respectively) by dissolving in ultrapure water (Millipore).

The experiments were controlled with a potentiostat (FHI, E-Lab). For the partial electronic compensation of the cell resistance, an NID was inserted between the WE and the potentiostat. The implemented electronic circuit is shown in Figure 1b. Input and output voltages are related by $U_{\text{out}} = U_{\text{in}} + (R_1 R_3 / R_2) I$.

2.2. Results. IO_4^- reduction on Au electrodes in neutral base electrolyte solution possesses the typical characteristics of an N–NDR oscillator.⁴⁹ At low electrolyte resistivity or, more generally, low cell resistance, the stationary polarization curve possesses the form of an N, the middle branch of which obviously exhibits an NDR. Upon gradually increasing the cell resistance, oscillations develop around the NDR branch. For even higher cell resistance, the current–voltage curve becomes bistable. With our electrochemical cell, a bistable response (with oscillations close to the positive end of the bistable voltage region) was, e.g., obtained with 3 mM NaClO_4 base electrolyte and 2 mM NaIO_4 .⁴⁵ In this case, the cell resistance, R_{Ω} , amounted to 1 k Ω . Figure 2 displays the positive scan direction of a cyclic voltammogram obtained in the same electrolyte, but

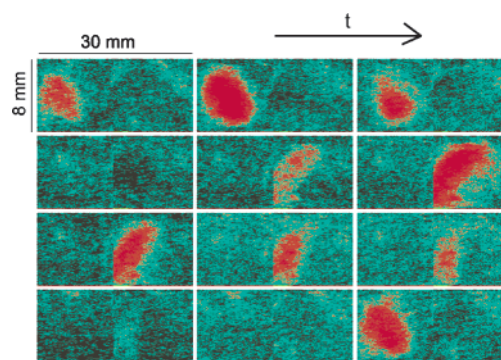


Figure 3. SPR images of the Au WE for fixed applied voltage during two oscillation periods of the current density ($U = -0.571 \text{ V}$, time between successive images = 0.3 s; for other parameters, see Figure 2).

with electronic compensation of $R_e = -800 \text{ }\Omega$ of the cell resistance by means of the NID. Obviously, the system was rendered oscillatory, the oscillations occurring around the NDR branch. It should be noted that there was a small hysteresis between the forward (increasing overvoltage) and backward scans, the oscillations developing much more easily on the backward than on the forward scan. This observation points to complications at positive potentials, such as adsorption of species with a subsequent reaction. We avoided these complications by always starting from voltage values at the negative end, i.e., from the passive state. In this way, oscillations were reproducibly obtained.

Figure 3 shows a series of SPR images that were recorded at a fixed value of the externally applied voltage, U , within the oscillatory region during two oscillation periods of the current density. First, we notice that the oscillation is clearly accompanied by pronounced changes in the optical properties of the interface, which give rise to a significant contrast in the series of images. Regions that appear red have a higher current density than the blackish-green ones. Second, and most strikingly, the oscillations are not uniform in space. Rather, during one oscillation of the current, only half of the electrode is activated, the two halves becoming active alternately. In the low current phase of the oscillations, the electrode takes on a quasi-uniform state. Obviously, the spatial symmetry along the long side of the electrode is broken, whereas the short side exhibits only minor variations at the electrode edges. This was the case throughout the potential interval in which pattern formation occurred. It is, thus, advantageous to represent the dynamics in x – t plots, whereby each spatial profile represents the averaged SPR image intensity along the short direction of the electrode.

To obtain an overview of the different patterns that establish at different values of the external voltage, SPR images were recorded during a slow voltage scan. Figure 4 displays three such x – t plots with corresponding time series of the global current. The first set of data (Figure 4a) was obtained close to the negative end of the oscillatory region, where the oscillations set in with a large amplitude and are relaxation-like and simple periodic. The corresponding x – t plot exhibits oscillations that seem to be restricted to about two-thirds of the electrode, the other one-third of the electrode staying essentially stationary. The last x – t plot (Figure 4c) was taken close to the positive end of the oscillatory region, at which the oscillations are harmonic and set in with a small amplitude, as characteristic for a supercritical Hopf bifurcation. The spatio-temporal dynamics have the same characteristics that were discussed above for the stationary experiment: The two halves of the electrode oscillate alternately in a harmonic manner, the resulting pattern

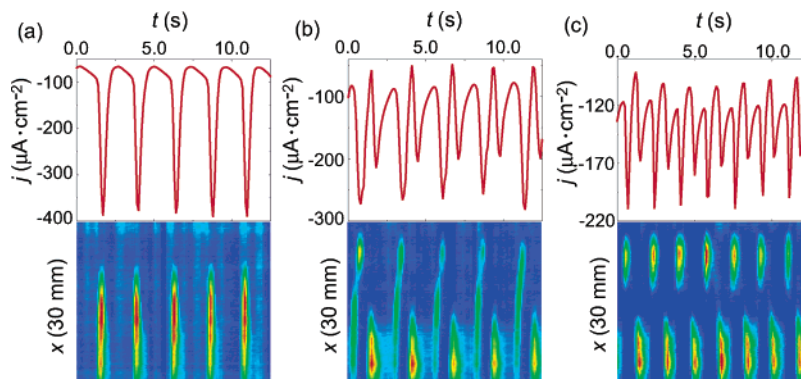


Figure 4. Patterns during slow voltage scans (1 mV/s) in the three different regions of the externally applied voltage indicated in Figure 2. Figures 4a–c correspond to regions a–c in Figure 2, respectively. Parameters are the same as those in Figure 2.

being reminiscent of a standing wave. Note, however, that the oscillations on the two sides are not perfectly symmetric, which causes a period-2 oscillation of the global current density. These nearly symmetric, standing-wave-type patterns were robust in a wide voltage interval.

Obviously, there is a qualitative transition between the simple periodic oscillations at the negative end of the oscillatory region and the period-doubled behavior on its positive side. This transition is mediated via a mixed behavior, which is depicted in Figure 4b. Every second oscillation of the global current density is accompanied by a structure that could be described as a pulselike motion from the originally oscillating side to the other side, or, equivalently, as an asymmetric standing wave, whose nodal point is pushed off the center of the electrode. Between two of these asymmetric standing wave oscillations, there is a localized oscillation on the side of the electrode that predominantly oscillates at more negative values of the applied voltage (Figure 4a).

The presented data clearly exhibit self-organized structures stemming from spatial symmetry breaking. Among them are certainly the standing-wave-type patterns at low values of the overpotential (Figure 4c). However, as already pointed out, the parts to the left and right of the nodal line in the standing wave regime are not perfectly symmetric. It seems to be obvious that these asymmetries result from (to some extent, unavoidable) imperfections in the experimental setup. The sources of these intrinsic inhomogeneities are the following: (1) The electrode surface is not completely uniform. (2) The transport to the electrode is maintained by convective flow, stemming from gas bubble stirring inducing a nonideal convection; recall also that the electrode extends over the entire bottom of the rectangular box with insulating walls connecting electrode and cell. As already mentioned, this geometry was chosen to minimize effects of an inhomogeneous potential distribution; however, this is done at the expense of a uniform transport, e.g., transport of IO_4^- ions to the boundary regions of the WE is certainly less effective than to the WE center. (3) The RE could not be placed centrally with respect to the long side of the electrode, resulting in different potential drops through the electrolyte between different locations of the electrode and the RE. Intuitively, one would expect that the worse transport gives rise to the more passive regions close to the electrode border (cf. Figure 3), and the asymmetric position of the RE is responsible for the electrode oscillating quasi-homogeneously only in two-thirds of the domain at high values of U , rather than in the entire domain (cf. Figure 4a). For other features, especially the alternation of the pulselike structures or asymmetric standing waves with the localized oscillations (cf. Figure 4b), it is even hard to make an intuitive guess whether the basic pattern is

truly self-organized or whether it is qualitatively influenced by the external inhomogeneities. To obtain further insight into the origin of the various observed features, a theoretical study with a generic N–NDR oscillator was carried out, which is presented in the following section.

3. Theory

3.1. Model. We are going to study the dynamics of the prototype N–NDR oscillator introduced in refs 50–52 under NGC, focusing on spatial instabilities of limit cycles. As discussed above, the chosen dimensions of the WE-allowed pattern formation effectively only in 1d. The chosen geometry of the WE and the surrounding insulator is suitably modeled using no-flux boundary conditions. The two essential variables in the prototype N–NDR oscillator are the double-layer potential, comprising the activatory variable, and the concentration of the reaction species in the reaction plane, which will be denoted by c , which is responsible for the negative feedback. The transport processes acting on the concentration of the reacting species parallel to the electrode, migration and diffusion, are neglected in the following. This is well justified since the migration coupling acting on the activator variable, ϕ_{DL} , is much faster than diffusion of the inhibitor, c . It is well known that the spatial coupling on the inhibitor can be neglected in this situation.

Recalling the derivation of the concentration dynamics given in ref 50 and using the general expression for the double-layer dynamics derived in ref 43, the dynamical system describing pattern formation in the prototype N–NDR oscillator is

$$C_{\text{DL}} \frac{\partial \phi_{\text{DL}}}{\partial t} = -i_r + \frac{\sigma}{w(1+\gamma)} (U - \phi_{\text{DL}}) + \frac{\sigma\gamma}{w(1+\gamma)} (\langle \phi_{\text{DL}} \rangle - \phi_{\text{DL}}) - \sigma \left(\frac{\partial \phi}{\partial z} - \frac{\phi}{w} \right) \Big|_{\text{WE}} \quad (1)$$

$$\frac{\delta}{2} \frac{\partial c}{\partial t} = \frac{1}{nF} i_r + \frac{D}{\delta} (c^b - c) \quad (2)$$

with

$$\gamma = R_e/R_\Omega$$

C_{DL} denotes the specific capacity of the double layer; i_r is the (negative) reduction current that is modeled by a cubic expression in ϕ_{DL} (s.b.). σ is the conductivity of the electrolyte. L denotes the width of the WE, and w is the distance between WE and CE (cf. Figure 5).

The last term in the double-layer equation describes the migration coupling. ϕ denotes the potential in the electrolyte,

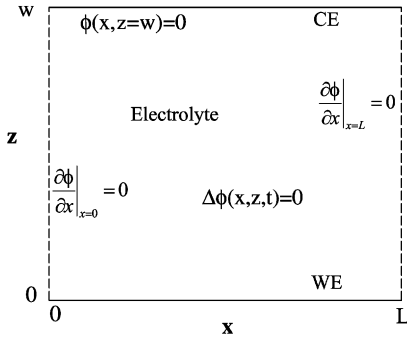


Figure 5. 2d cell geometry and boundary conditions. The boundary condition at the WE is given by eq 1.

TABLE 1: Parameter Values Used in Equations 3 and 4

$\epsilon = 0.0005$	$\sigma = 0.2$
$\beta = 3$	$k_0 = 7.2932 \times 10^{-5}$
$k_1 = 472.5$	$k_2 = 5.5932 \times 10^4$
$\gamma = -0.7$	

which obeys Laplace's equation, and $\partial/\partial z$ is the derivation in the direction perpendicular to the WE, where z points into the electrolyte. The coordinate parallel to the WE is denoted x . The coupling between the different locations, x_i , at the electrode is mediated through the electric potential in the electrolyte; a change of $\phi(x, z = \text{WE})$ at a particular position changes ϕ in the entire electrolyte and, thus, also $\partial\phi/\partial z|_{z=\text{WE}}$. Mathematically, the coupling is brought about by Laplace's equation. δ denotes the thickness of the diffusion layer. n is the number of electrons transferred per reaction. F is Faraday's constant, and D is the diffusivity of the reacting species in the electrolyte. c^b is the bulk concentration of c .

Equations 1 and 2 are used in their dimensionless form in the following. The transformations of the variables and parameters are given in the Appendix. The resulting equations read (the new variables and parameters are relabeled to the old ones for clarity)

$$\epsilon \frac{\partial \phi_{\text{DL}}}{\partial t} = -i_r + \frac{\sigma}{\beta(1+\gamma)}(U - \phi_{\text{DL}}) + \frac{\sigma\gamma}{\beta(1+\gamma)}(\langle \phi_{\text{DL}} \rangle - \phi_{\text{DL}}) - \frac{\sigma}{\beta} \left(\frac{\partial \phi}{\partial z} - \phi \right) \Big|_{\text{WE}} \quad (3)$$

$$\frac{\partial c}{\partial t} = i_r + 1 - c \quad (4)$$

with

$$i_r = ck_0(\phi_{\text{DL}}^3 + k_1\phi_{\text{DL}}^2 + k_2\phi_{\text{DL}})$$

and the boundary conditions

$$\frac{\partial \phi_{\text{DL}}}{\partial x} \Big|_{x=0,\pi} = \frac{\partial c}{\partial x} \Big|_{x=0,\pi} = \frac{\partial \phi}{\partial x} \Big|_{x=0,\pi} = \phi|_{\text{CE}} = 0 \quad (5)$$

The Laplace equation is valid in the entire electrolyte. The dynamics at the CE are neglected. The only time-dependent boundary condition is given by eq 3. The parameters, k_i , were fitted to the reduction of peroxodisulfate on Ag, yielding the values given in Table 1⁵² (ϕ_{DL} is measured with respect to the equilibrium potential). The other parameter values are determined by physical constants and the experimental parameters used and are also compiled in Table 1.

Figure 6a displays the current–potential characteristic of the N–NDR system, together with a representative load line for the parameters given in Table 1. Since the parameters are fitted

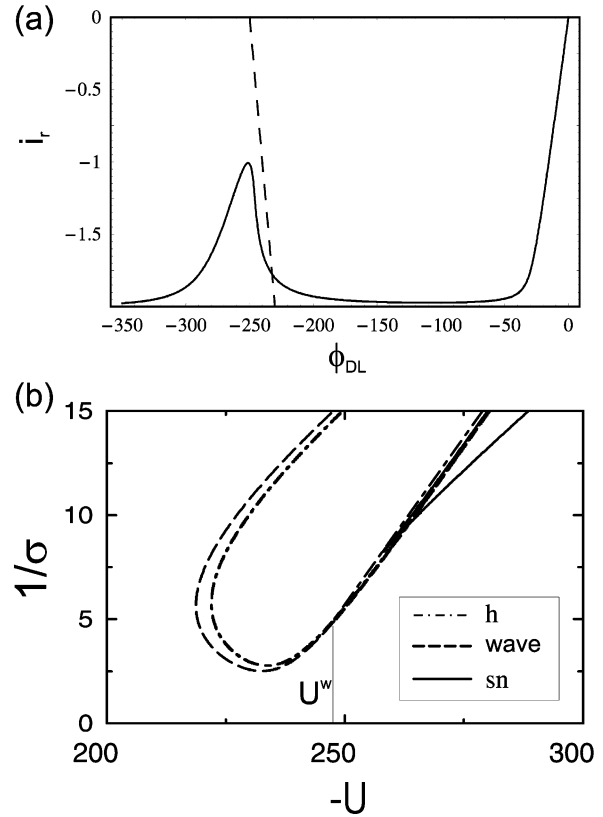


Figure 6. (a) N-shaped current–potential characteristic (solid line) together with a load line that intersects the N–NDR characteristic on the branch of negative differential resistance (dashed line). (b) Saddle-node (solid line), Hopf (dashed–dotted line), and wave (dashed line) bifurcations in the $(1/\sigma-U)$ -parameter plane. $-U$ is plotted to obtain the familiar scale (increasing overpotential with increasing $-U$). Parameters are the same as those given in Table 1.

to the reduction of peroxodisulfate on Ag, the reaction current and the applied voltages are negative. For these parameter values, the model displays an NDR for ϕ_{DL} approximately between -250 and -100 .

3.2. Methods. The Laplace equation in the electrolyte can be solved by a series expansion in harmonics and hyperbolics.⁵³ The relation between ϕ_{DL} and ϕ is given by the potentiostatic control condition. If ϕ_{DL} is also expanded in a Fourier series

$$\phi_{\text{DL}}(x,t) = \sum_{n=0}^{\infty} a_n^{\phi_{\text{DL}}} \cos nx \quad (6)$$

the dynamics of ϕ_{DL} in Fourier space is given by (see ref. 24 for a more detailed discussion)

$$\epsilon \dot{a}_0^{\phi_{\text{DL}}} = \int_0^\pi i_r dx + \frac{\sigma}{\beta(1+\gamma)}(U - a_0^{\phi_{\text{DL}}}) \quad (7)$$

$$\epsilon \dot{a}_n^{\phi_{\text{DL}}} = \int_0^\pi i_r \cos nx dx - \sigma n \coth(\beta n) a_n^{\phi_{\text{DL}}} \quad (8)$$

Due to the strong damping of higher modes for the chosen system size, it was sufficient to work with 15 cosine modes. Equations 7 and 8 were analyzed using the bifurcation analysis software AUTO.⁵⁴ Simulations were performed using the Livermore Solver for Ordinary Differential Equations (lsode), with an error tolerance of 10^{-8} .⁵⁵

3.3. Bifurcation Analysis and Simulations. A linear stability analysis of the homogeneous fixed point of eqs 3 and 4 was performed by Christoph.^{32,48} If σ and U are chosen such that the system has one fixed point on the branch of negative

differential resistance of the current–potential characteristic (cf. Figure 6a), the following statements can be made regarding the basic instabilities. (For other values of σ , the load line will display three intersections with the current–potential characteristic and bistability between the active state and passive state will be observed, which is not of interest here.) If the dynamics of the activator, ϕ_{DL} , is faster than a threshold, the steady state is oscillatory unstable. This threshold is independent of the global coupling. The oscillatory motion stays homogeneous for weak global coupling. Inhomogeneous oscillations will be observed for stronger NGC.

Figure 6b displays the locations of saddle-node, Hopf, and wave bifurcations (a nontrivial mode becomes oscillatory unstable) of eqs 3 and 4 in the $(1/\sigma-U)$ parameter plane. Since we are interested in oscillatory solutions and no bistability is found in the system for $\sigma \gtrsim 0.15$, $\sigma = 0.2$ is used in the following. At this NGC strength, the homogeneous steady state is always destabilized in a wave bifurcation before homogeneous oscillations bifurcate from the unstable fixed point (cf. Figure 6b). We denote the point of the wave bifurcation at lower U as U^w .

In the following, the bifurcation scenario as a function of U is given and is illustrated with numerical simulations. The other parameters are fixed at the values mentioned above.

Bifurcations displayed by eqs 3 and 4 as a function of U are shown in Figure 7 in a projection on the $(\max(\langle i_r \rangle)-U)$ plane, where $\langle i_r \rangle := \int_0^\pi i_r dx$. The bifurcation diagram was calculated using seven cosine modes. The system exhibits one stable homogeneous stationary fixed point (solid line) for applied voltages $U \lesssim -248$ and $U \gtrsim -219$. As already shown in Figure 6b, the fixed point loses stability in wave bifurcations at lower and higher applied voltages. The unstable homogeneous oscillations bifurcate from the unstable steady state just after the respective wave bifurcation at lower and higher values of the applied voltage, respectively. The increase of $\max(\langle i_r \rangle)$ at the nontrivial Hopf bifurcation at U^w is very steep until a plateau is reached, which is attributed to the complex phase space structure at $U = U^w$, briefly discussed below.

The bifurcations are going to be discussed in the order of decreasing applied voltage, i.e., increasing overpotential. The oscillatory instability with wavenumber one at $U \approx -219$ is supercritical, and a branch of stable standing wave solutions is born (filled circles). An example of the observed spatio-temporal motion is given in Figure 8a. As can be seen in the second plate of Figure 8a, the oscillation amplitude of the homogeneous mode of the double-layer potential, $a_0^{\phi_{DL}}$, is small compared to the amplitude of the first cosine mode, $a_1^{\phi_{DL}}$. Still, the amplitude of the homogeneous mode is not equal to zero. Consequently, the pattern shown in Figure 8a does not resemble a standing wave in the strict sense and is, thus, often termed anti-phase oscillation. The oscillation frequency of the homogeneous mode is twice that of the first cosine mode since $\langle \phi_{DL} \rangle$ is only sensitive to $|a_1^{\phi_{DL}}|$. This frequency-doubled behavior is retained in the oscillations of the averaged reaction current density that are of relatively small amplitude.

The branch of stable standing wave solutions loses stability and gives rise to qualitatively new dynamics (filled triangles) in a supercritical pitchfork bifurcation of limit cycles (one Floquet-multiplier crosses +1) at $U = U^a$. An example of the resulting pattern at a finite distance from the bifurcation point is shown in Figure 8b. Most remarkable is the spatial asymmetry in the spatio-temporal motion. The nodal line of the standing wave that is positioned at $\pi/2$ for $U > U^a$ moves closer to one of the borders. Additionally, the symmetry regarding the

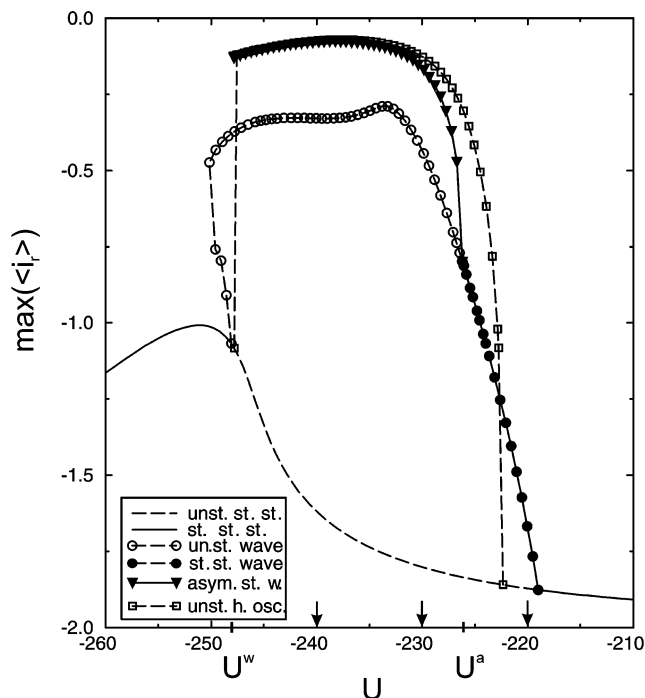


Figure 7. Bifurcation diagram of the prototype N-NDR oscillator under NGC. Displayed is the average (maximum) reaction current density, $\max(\langle i_r \rangle)$, as a function of the applied voltage, U . Going down from more positive voltages, the homogeneous steady state (solid line) loses stability in a supercritical wave bifurcation. A more complex asymmetric spatio-temporal pattern (filled triangles, cf. Figure 8b) bifurcates from the branch of standing wave solutions (filled circles, cf. Figure 8a) in a supercritical pitchfork bifurcation of limit cycles at $U = U^a$. This branch terminates in a phase space region with complex structure discussed in the text. The unstable homogeneous oscillations (open squares) branch from the unstable homogeneous steady state (dashed line) after the wave bifurcation and return to the fixed point at lower voltages before the following subcritical wave bifurcation (open circles) at $U = U^w$. A set of unstable inhomogeneous limit cycles existing in a small U interval is not shown here. Note that solutions were calculated at more U values, but are omitted here for clarity. The arrows indicate the points at which spatio-temporal simulations are presented in Figure 8. For parameters, see Table 1.

separation by half an oscillation period of the ϕ_{DL} maxima appearing at the borders is also removed, such that the excitations at the borders appear shortly one after the other, separated by passive intervals (high $|\phi_{DL}|$). We term this pattern *asymmetric standing wave*. This quite unusual behavior becomes clearer if one considers the first Fourier modes given in plate two of Figure 8b. The first cosine mode oscillates symmetrically to zero as expected. The asymmetry stems from the interplay of the first mode with the homogeneous mode. The homogeneous mode displays a two-peaked oscillation. The highest peak coincides with the maximum amplitude of the first mode. The maximum amplitude of the first mode with the opposite sign, corresponding to the other half of the electrode, occurs on the downward flank of the homogeneous mode. Consequently, the sum of homogeneous and first mode is smaller, leading to an asymmetric nodal line.

The oscillation frequencies of the homogeneous and the spatial modes coincide for asymmetric standing waves. Starting from the bifurcation point, the amplitudes of the two $a_0^{\phi_{DL}}$ maxima in one period of $a_1^{\phi_{DL}}$ evolve in different directions. Additionally, the lower maximum moves closer to the previous absolute one. Thus, a smooth transition from standing waves to asymmetric standing waves is provided. Note also that the two-peaked structure of the homogeneous double-layer

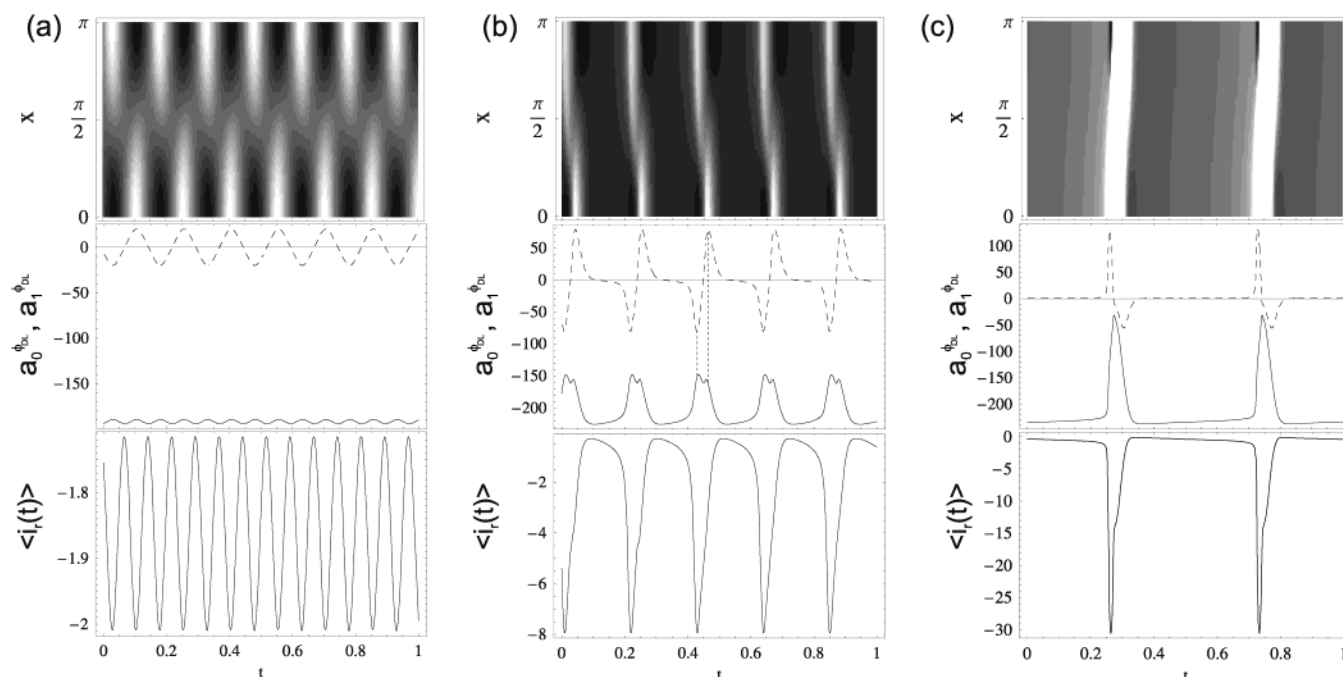


Figure 8. (a) Standing wave pattern at $U = -220$. (b) Asymmetric standing wave at $U = -230$. (c) Pulselike pattern at $U = -240$. First plates; $\phi_{DL}(x, t)$; second plates; homogeneous ϕ_{DL} mode, $a_0^{\phi_{DL}}(t)$, (solid line) and first cosine mode, $a_1^{\phi_{DL}}(t)$, (dashed line); third plates; $\langle i_i(t) \rangle$. For parameters, see Table 1. A linear gray scale map was used; white corresponds to low $|\Phi_{DL}|$ (active state) and black to the maximal $|\Phi_{DL}|$ value (passive state), respectively.

potential–time series is not retained in the mean reaction current density, pointing to a nonvanishing contribution of capacitive currents.

At again lower applied voltages, the dynamics evolve continuously to a pulselike behavior, as shown in Figure 8c. The amplitude of the first cosine mode increases fast as soon as the vicinity of the unstable homogeneous fixed point is left and leads to the spatio-temporal impression of a pulselike motion. The pulselike pattern stems from an additional asymmetry in the first spatial modes, cf. the dashed line in plate two of Figure 8c. The current oscillations in this U -range exhibit long passive periods, which hints at a possible proximity of a homoclinic orbit since the stationary state is also passive. Comparing the current and potential values of the long passive phase with the respective values of the unstable fixed point further supports this hypothesis. The homogeneous fixed point is of the saddle-focus type at these parameter values, cf. Figure 7. The plane of the unstable focus is spanned by the first cosine modes of ϕ_{DL} and c , $a_1^{\phi_{DL}}$ and a_1^c , respectively. The trajectory is brought into the vicinity of the fixed point by the stable directions and spirals out in the $(a_1^{\phi_{DL}} - a_1^c)$ plane, which comprises the slow direction in phase space. Finally, an excursion in phase space is observed in which the inhomogeneous modes grow fast in the initial stage, and the pulselike motion is observed. It is argued in detail in a forthcoming publication that, indeed, a homoclinic connection terminates the branch of asymmetric standing wave solutions.

Decreasing the applied voltage further below U^w , the passive homogeneous steady state was found to be the only attractor.

4. Discussion

The experimental results summarized above show that the main effect of the NGC is to induce a spatial symmetry breaking in one spatial dimension, namely the longer direction of the electrode. The spatial bifurcations behind the different symmetry breakings were investigated in experiment and in a generic

model. Comparing the theoretical results with the experiments, there are striking corresponding features, but also some discrepancies, both of which will be elaborated in the following.

The existence of standing waves with wavenumber one in a voltage interval starting at the positive end of the oscillatory region is found in experiments and in simulations. The calculations confirm that these patterns emerge due to the presence of NGC and that the standing waves are born in a wave bifurcation. Note, however, that, in the calculations, the standing waves possess their maximal amplitude at the edges, while it is somewhere between $1/8$ and $1/4$ away from the edge in the experiments. It seems to be very likely that this discrepancy results from a lower transport of periodate to the edges of the electrode, compared with that of its central part (see above). It should be noted that standing waves were previously reported to exist in 1d in the model of the prototype N–NDR oscillator under NGC, using periodic boundary conditions,^{32,35} and in experiments during formic acid oxidation, using a ring WE with close RE.³⁷

The spatio-temporal dynamics in the standing wave regime possess a symmetry (which is not perfect in the experiments, due to the presence of inhomogeneities): The pattern is invariant upon reflection at the center of the electrode followed by a phase shift of 180° of the local period in time ($\phi_{DL}(x, t) = \phi_{DL}(x + \pi, t + T/2)$). This symmetry is broken again in the experiments, as well as in the simulations, closer to the negative end of the oscillatory region. Moreover, in simulations and experiments, the resulting dynamics exhibit asymmetric standing waves. Recalling that the model does not include any specific kinetics of the periodate reduction, which are still unknown, but describes the reaction current by a polynomial of third degree, the correspondence of this subtle feature impressively confirms that these features are generic and should exist in any N–NDR oscillator under NGC.

However, there are also discrepancies between the calculated dynamics and the experimental results, in particular in the

asymmetric standing wave and in the pulse regime. The experimental asymmetric standing waves alternate with localized oscillations on the side of the electrode on which the asymmetric oscillation emerges. Such a more complex succession of asymmetric and localized oscillations has not been observed in the theoretical investigations. There are different possible explanations for this discrepancy. Most important is the asymmetric position of the RE in experiment, which implies that the potential drops from the RE to different positions on the WE are different. Consequently, there is a small gradient in the effective resistance along the electrode which causes a slight shift in the homogeneous dynamics. Thus, the oscillation frequency might vary, and, as a consequence, only every second oscillation on one side is complemented by an asymmetric counterpart on the other side. Simulations with an asymmetrically placed RE were carried out by Birzu et al.,⁵⁶ using a model describing metal dissolution and a 1d ribbon electrode. The reaction dynamics and the cell geometry were different from the ones discussed in this contribution. However, it is remarkable that these simulations exhibit a pattern in which one side of the electrode oscillates with twice the frequency of the other side. This result is a hint that the position of the RE causes the main qualitative differences in the dynamic behavior between the experiments and the simulations. In view of the discussion of the impact of the asymmetrically placed RE on the dynamics, we would like to emphasize again that the symmetry breaking from the symmetric standing waves to the asymmetric standing waves was also found in the theory using a perfectly symmetric geometry and is, thus, not caused by the unavoidable nonuniformities present in any experiment. This discussion also shows how intricate the interaction between reaction kinetics, negative global coupling, and nonuniformities might be, which makes an interpretation of the origin of the patterns without accompanying calculations nearly impossible. Additionally, we cannot exclude that the experimentally observed additional localized oscillations are caused by reaction kinetics that are more complicated than the one of the generic N–NDR model.

In the immediate neighborhood of the negative end of the oscillatory regime, simple periodic oscillations were found in the experiments. About two-thirds of the electrode close to one side took part in the oscillations, the remaining one-third being practically stationary. In opposition to this, relaxation-like oscillations that resemble a pulse which travels across the entire electrode were found in the simulations. This apparent discrepancy between experiment and model could have two reasons. The spatial inhomogeneity during pulselike motion is only present with large amplitudes in the transition from active to passive phase and vice versa, cf. Figure 8c. The relaxation-like oscillations might require a better signal-to-noise ratio than that which is available in the experiments to distinguish between pulselike and homogeneous dynamics. Another possible explanation is that the sequence of Hopf and wave bifurcations at the lower U -boundary is reversed at different parameters, in the sense that the homogeneous steady state is first destabilized in a Hopf bifurcation, thus, giving rise to stable homogeneous oscillations. However, the relaxation-like form of the oscillations is observed in experiment and theory.

Christoph et al. observed target patterns in the generic N–NDR model under NGC, using periodic boundary conditions. Target patterns are the analogue of pulselike behavior in systems with periodic boundary conditions. Adding a reflected image of the pulselike behavior to Figure 8c to extend space to the interval from 0 to 2π , target patterns are obtained. The transition from standing waves to target patterns also involves

a symmetry-breaking bifurcation in systems with periodic boundary conditions, since the symmetry $\phi_{DL}(x, t) = \phi_{DL}(x + \pi, t + T/2)$ is lost at the transition. The bifurcation analysis performed here revealed the pitchfork bifurcation connecting these two states and that asymmetric standing waves precede pulselike motion coming from standing waves. Pulselike behavior in oscillatory reaction–diffusion systems with no-flux boundary conditions under global coupling was reported earlier.^{4,5} A systematic study of the bifurcations using continuation techniques has not been presented before.

Finally, we would like to comment on one more issue. The experiments discussed above were carried out with 2d rectangular electrodes. However, the spatial symmetry breaking induced by the negative global coupling took place almost exclusively in one spatial dimension, namely the longer side of the electrode. There are at least two possible explanations for this phenomenon: (a) Either the critical length beyond which the system is too small to allow for a nontrivial Hopf bifurcation is larger than the small side of the electrode or (b) the uniform surface could become unstable with respect to a symmetry breaking in either of the two spatial dimensions. The basin of attraction of the solution that exhibits a symmetry breaking into the smaller direction is, however, much smaller, such that it is much less likely to occur. Schöll and co-workers performed calculations on pattern formation in 2d semiconductor electrodes in the presence of global coupling.⁵⁷ They found that if the 1d symmetry breaking can occur in either of the directions, so-called edge oscillations are also stable, which can be most easily described by an oscillation of one-quarter of the electrode, i.e., a genuine 2d pattern. Our experiments showed that, at least for largely different lengths of the two electrode sides, edge oscillations are very unlikely. Calculations with the generic N–NDR model and a 2d electrode geometry are necessary to test whether this type of patterns exists at all in electrochemical systems and in which parameter range and for which aspect ratio of the electrode it is to be expected.

5. Conclusion

In this paper, we described pattern formation on a rectangular gold film electrode during periodate reduction in the presence of negative global coupling in experiment and theory, with special emphasis on the spatial bifurcations as a function of the applied voltage. The periodate reduction is a typical N-shaped negative differential resistance oscillator, but the underlying mechanisms are still unknown. The prototype N–NDR model is built on the most common electrochemical mechanisms for oscillatory behavior, and the reaction rate constants were fitted to model peroxodisulfate reduction but agree with experimental data obtained during periodate reduction. Thus, the results presented here are expected to be representative for all N–NDR oscillators.

The negative global coupling was accomplished using an electronic device that acts like a negative ohmic resistor. This is the only way in which a strictly negative global coupling can be imposed on an electrochemical cell (using a Haber–Lugin capillary is an alternative only for ideal 1d ring electrodes). Its relevance lies in the fact that the automatic IR compensation that many commercial potentiostats offer also acts like an external negative ohmic resistor. From the critical coupling strength on, the negative global coupling leads to a spatio-temporal symmetry breaking, thus, impeding the existence of uniformly reacting electrodes.

The following sequence of stable attractors was observed with decreasing applied voltage with otherwise fixed parameters,

TABLE 2: Physical Parameter Values Used in the N–NDR Dynamics

$L = 1 \text{ cm}$	$C_{\text{DL}} = 0.2 \text{ F/m}$
$w = 1.05 \text{ cm}$	$D = 10^{-9} \text{ m}^2/\text{s}$
$\delta = 10^{-5} \text{ m}$	$U \in [-1, -3] \text{ V}$
$c^b = 0.05 \text{ mol/m}^3$	$\sigma = 0.065 (\Omega \text{ m})^{-1}$
$f = 38 \text{ V}^{-1}$	

especially fixed negative global coupling strength. The homogeneous steady state loses stability in a supercritical wave bifurcation, leading to standing waves. A secondary (symmetry breaking) supercritical pitchfork bifurcation identified in the model gives rise to asymmetric standing waves, reported here for the first time. The dynamics underlying the occurrence of asymmetric standing waves could be clarified. Asymmetric standing waves transform to pulselike behavior. Approaching the homogeneous passive state at lower U , the spatio-temporal dynamics become relaxation-like, which hampers the distinction between pulselike behavior and homogeneous oscillations in experiments. The remarkable correspondence between the general N–NDR model and the “black-box” N–NDR experimental oscillator underlines the generality of the presented results. Some of the fine structure of the experimental patterns was not reproduced in the simulations and is most likely due to unavoidable nonuniformities in the experimental setup.

The applicability of a negative impedance device to impose strictly negative global coupling on two-dimensional electrodes is thus demonstrated and opens the way to future studies on strict global coupling imposed on two-dimensional geometries.

Acknowledgment. Financial support from the Deutsche Forschungsgemeinschaft in the framework of the Sonderforschungsbereich 555 “Complex Nonlinear Processes”, project B4, is gratefully acknowledged.

Appendix

The set of equations describing the dynamics in the N–NDR system in physical units given in section 3.1, eqs 1 and 2, can be cast into dimensionless form. With the transformations of the variables

$$2D\delta^{-2}t \rightarrow t$$

$$c \rightarrow c/c^b$$

$$\phi_{\text{DL}} \rightarrow f\phi_{\text{DL}}$$

$$x \rightarrow x\pi/L$$

$$z \rightarrow z/w$$

(all voltages are scaled accordingly, $f = nF/RT$, where R denotes the gas constant, and T is the temperature) and the definitions of the parameters

$$\epsilon = 2C_{\text{DL}}(c^b nF\delta f)^{-1}$$

$$\sigma \rightarrow \sigma\pi\delta(nFc^b DLf)^{-1}$$

$$U \rightarrow fU$$

$$\beta = \pi Lw^{-1}$$

eqs 1 and 2 transform to the dimensionless dynamical system given by eqs 3 and 4. The physical parameter values used are given in Table 2. The resulting dimensionless parameters are compiled in Table 1. The constants, k_i , were fitted to experimental data obtained during $\text{S}_2\text{O}_8^{2-}$ reduction on Ag.⁵²

References and Notes

(1) Barelko, V.; Kurochka, I. I.; Merzhanov, A. G.; Shkadinskii, K. G. *Chem. Eng. Sci.* **1977**, *33*, 805.

- (2) Zhukov, S. A.; Barelko, V. V. *Sov. J. Chem. Phys.* **1984**, 1982(4), 883.
- (3) Lobban, L.; Philippou, G.; Luss, D. *J. Phys. Chem.* **1989**, *93*, 733.
- (4) Mertens, F.; Imbihl, R.; Mikhailov, A. *J. Chem. Phys.* **1993**, *99*, 8668.
- (5) Middya, U.; Graham, M. D.; Luss, D.; Sheintuch, M. *J. Chem. Phys.* **1993**, *98*, 2823.
- (6) Mertens, F.; Imbihl, R.; Mikhailov, A. *J. Chem. Phys.* **1994**, *101*, 9903.
- (7) Falcke, M.; Engel, H. *Phys. Rev. E: Stat. Phys., Plasmas, Fluids, Relat. Interdiscip. Top.* **1994**, *50*, 1353.
- (8) Rose, K. C.; Battogtokh, D.; Mikhailov, A. S.; Imbihl, R.; Engel, W.; Bradshaw, A. M. *Phys. Rev. Lett.* **1996**, *76*, 3582.
- (9) Vesper, G.; Mertens, F.; Mikhailov, A. S.; Imbihl, R. *Phys. Rev. Lett.* **1993**, *71*, 935.
- (10) Falcke, M.; Engel, H. *Phys. Rev. E: Stat. Phys., Plasmas, Fluids, Relat. Interdiscip. Top.* **1997**, *56*, 635.
- (11) Elmer, F. J. *Phys. Rev. A: At., Mol., Opt. Phys.* **1990**, *41*, 4174.
- (12) Schöll, E. *Nonlinear Spatio-Temporal Dynamics and Chaos in Semiconductors*; Cambridge Nonlinear Science Series 10; Cambridge University Press: Cambridge, 2001.
- (13) Seung, K. H.; Kurrer, C.; Kuramoto, Y. *Phys. Rev. Lett.* **1995**, *75*, 3190.
- (14) Schebesch, I.; Engel, H. In *Self-Organization in Activator-Inhibitor Systems: Semiconductors, Gas-Discharges and Chemical Active Media*; Engel, H., Niedernostheide, F.-J., Purwins, H.-G., Schöll, E., Eds.; Wissenschaft & Technik-Verlag: Berlin, 1996; p 120.
- (15) Battogtokh, D.; Mikhailov, A. S. *Physica D (Amsterdam)* **1996**, *90*, 84.
- (16) Battogtokh, D.; Preusser, A.; Mikhailov, A. S. *Physica D (Amsterdam)* **1997**, *106*, 327.
- (17) Franceschini, G.; Bose, S.; Schöll, E. *Phys. Rev. E: Stat. Phys., Plasmas, Fluids, Relat. Interdiscip. Top.* **1999**, *60*, 5426.
- (18) Vanag, V. K.; Lingfa, Y.; Dolnik, M.; Zhabotinsky, A. M.; Epstein, I. R. *Nature* **2000**, *406*, 389.
- (19) Bertram, M.; Mikhailov, A. S. *Phys. Rev. E: Stat. Phys., Plasmas, Fluids, Relat. Interdiscip. Top.* **2001**, *63*, 066102.
- (20) Kim, M.; Bertram, M.; Pollmann, M.; Oertzen, A.; Mikhailov, A. S.; Rotermund, H. H.; Ertl, G. *Science* **2001**, *292*, 1357.
- (21) Beck, O.; Aman, A.; Schöll, E.; Socolar, J. E. S.; Just, W. *Phys. Rev. E: Stat. Phys., Plasmas, Fluids, Relat. Interdiscip. Top.* **2002**, *66*, 016213.
- (22) Just, W.; Benner, H.; Reibold, E. *Chaos* **2003**, *13*, 259.
- (23) Imbihl, R.; Ertl, G. *Chem. Rev.* **1995**, *95*, 697.
- (24) Krischer, K. In *Advances in Electrochemical Science and Engineering*; Alkire, R. C., Kolb, D. M., Eds.; Wiley-VCH: 2003; p 89.
- (25) Ertl, G. *Science* **1991**, *254*, 1750.
- (26) Beta, C.; Bertram, M.; Mikhailov, A. S.; Rotermund, H. H.; Ertl, G. *Phys. Rev. E: Stat. Phys., Plasmas, Fluids, Relat. Interdiscip. Top.* **2003**, *67*, 046224.
- (27) Bertram, M.; Beta, C.; Pollmann, M.; Mikhailov, A. S.; Rotermund, H. H.; Ertl, G. *Phys. Rev. E: Stat. Phys., Plasmas, Fluids, Relat. Interdiscip. Top.* **2003**, *67*, 036208.
- (28) Wacker, A.; Schöll, E. *Z. Phys. B: Condens. Matter* **1994**, *93*, 431.
- (29) Plenge, F.; Rodin, P.; Schöll, E.; Krischer, K. *Phys. Rev. E: Stat. Phys., Plasmas, Fluids, Relat. Interdiscip. Top.* **2001**, *64*, 056229.
- (30) Falcke, M.; Engel, H.; Neufeld, M. *Phys. Rev. E: Stat. Phys., Plasmas, Fluids, Relat. Interdiscip. Top.* **1995**, *52*(1), 763.
- (31) Grauel, P.; Christoph, J.; Flätgen, G.; Krischer, K. *J. Phys. Chem. B* **1998**, *102*, 10264.
- (32) Christoph, J.; Otterstedt, R. D.; Eiswirth, M.; Jaeger, N. I.; Hudson, J. L. *J. Chem. Phys.* **1999**, *110*, 8614.
- (33) Mazouz, N.; Flätgen, G.; Krischer, K.; Kevrekidis, I. G. *J. Electrochem. Soc.* **1998**, *145*, 2404.
- (34) Otterstedt, R. D.; Plath, P. J.; Jaeger, N. I.; Hudson, J. L. *Faraday Trans.* **1996**, *92*, 2933.
- (35) Christoph, J. *Musterbildung auf Elektrodenoberflächen*. Ph.D. thesis, Freie Universität; Berlin, 1999.
- (36) Christoph, J.; Strasser, P.; Eiswirth, M.; Ertl, G. *Science* **1999**, *284*, 291.
- (37) Strasser, P.; Christoph, J.; Lin, W.-F.; Eiswirth, M.; Hudson, J. L. *J. Phys. Chem. A* **2000**, *104*, 1854.
- (38) Grauel, P.; Krischer, K. *Phys. Chem. Chem. Phys.* **2001**, *3*, 2497.
- (39) Grauel, P.; Varela, H.; Krischer, K. *Faraday Discuss.* **2001**, *120*, 165.
- (40) Birzu, A.; Green, B. J.; Otterstedt, R. D.; Hudson, J. L.; Jaeger, N. I. *Z. Phys. Chem.* **2002**, *216*, 459.
- (41) Lee, J.-Y.; Christoph, J.; Strasser, P.; Eiswirth, M.; Ertl, G. *Phys. Chem. Chem. Phys.* **2003**, *5*, 935.
- (42) Birzu, A.; Plenge, F.; Jaeger, N. I.; Hudson, J. L.; Krischer, K. *J. Phys. Chem.* **2003**, *107*, 5825.
- (43) Krischer, K.; Varela, H.; Birzu, A.; Plenge, F.; Bonnefont, A. *Electrochim. Acta* **2003**, *49*, 103.

- (44) Plenge, F. Theory of electrochemical pattern formation under global coupling. Ph.D. thesis, Technische Universität; Berlin, 2003.
- (45) Li, Y.-J. Adsorption processes and spatiotemporal pattern formation during electrochemical reaction on Au(111) film electrodes. Ph.D. Thesis, Freie Universität; Berlin, 2003.
- (46) Martin, A.; Lerch, M.; Simmonds, P.; Eaves, L. *Appl. Phys. Lett.* **1994**, *64*, 1248.
- (47) Flätgen, G.; Krischer, K.; Pettinger, B.; Dobelhofer, K.; Junkes, H.; Ertl, G. *Science* **1995**, *269*, 668.
- (48) Christoph, J.; Eiwirth, M. *Chaos* **2002**, *12*, 215.
- (49) Li, Y.-J.; Oslonovitch, J.; Mazouz, N.; Plenge, F.; Krischer, K.; Ertl, G. *Science* **2001**, *291*, 2395.
- (50) Koper, M. T. M.; Sluyters, J. H. J. *J. Electroanal. Chem.* **1991**, *303*, 73.
- (51) Koper, M. T. M. *Electrochim. Acta* **1992**, *37*, 1771.
- (52) Mazouz, N.; Krischer, K.; Flätgen, G.; Ertl, G. *J. Phys. Chem. B* **1997**, *101*, 2403.
- (53) Flätgen, G.; Krischer, K. *J. Chem. Phys.* **1995**, *103*, 5428.
- (54) Doedel, E. J.; Kevernez, J. P. AUTO: Software for continuation and bifurcation problems in ordinary differential equations; Applied mathematics report, California Institute of Technology: Pasadena, 1986.
- (55) Hindmarsh, A. C. In *Scientific Computing*; Stepleman, R. S., Ed.; IMACS Transactions on Scientific Computation 1; North-Holland: Amsterdam, 1983; p 55.
- (56) Birzu, A.; Green, B. J.; Otterstedt, R. D.; Jaeger, N. I.; Hudson, J. L. *Phys. Chem. Chem. Phys.* **2000**, *2*, 2715.
- (57) Bose, S.; Rodin, P.; Schöll, E. *Phys. Rev. E: Stat. Phys., Plasmas, Fluids, Relat. Interdiscip. Top.* **2000**, *62*, 1778.